https://doi.org/10.1016/j.compscitech.2020.108273

Temperature Effect on All-inkjet-printed Nanocomposite Piezoresistive Sensors for Ultrasonics-based Health Monitoring

Pengyu Zhou[a‡], Wuxiong Cao[a,b‡], Yaozhong Liao[a‡], Kai Wang[a], Xiongbin Yang[a], Jianwei Yang[a], Yiyin Su[a], Lei Xu[a], Li-min Zhou[c], Zhong Zhang[d] and Zhongqing Su[a,e]*

[a] Department of Mechanical Engineering,
The Hong Kong Polytechnic University, Kowloon, Hong Kong SAR

[b] School of Astronautics,
Harbin Institute of Technology, Harbin 150080, PR China

[c] School of System Design and Intelligent Manufacturing,
Southern University of Science and Technology, Shenzhen 518055, PR China

[d] CAS Key Laboratory of Nanosystem and Hierarchical Fabrication,
National Center for Nanoscience and Technology, Beijing 100190, PR China

[e] The Hong Kong Polytechnic University Shenzhen Research Institute,
Shenzhen 518057, PR China

submitted to ***Composites Science and Technology***

(initially submitted on 23rd April 2020; revised and resubmitted on 25th May 2020)

‡ These authors contributed equally.
* To whom correspondence should be addressed. Tel.: +852-2766-7818, Fax: +852-2365-4703,
Email: zhongqing.su@polyu.edu.hk (Prof. Zhongqing Su, *Ph.D.*)

Abstract

The sensing performance of nanocomposite piezoresistive sensors in acquiring broadband acousto-ultrasonic wave signals is scrutinized in an extensive regime of temperature variation from –60 to 150 ºC, which spans the thermal extremes undergone by most aircraft and spacecraft. Ultralight and flexible, the sensors are all-inkjet-printed using a drop-on-demand additive manufacturing approach, and then optimized sensitive to the ultraweak disturbance induced by acousto-ultrasonic waves in virtue of quantum tunneling effect. Under high-intensity thermal cycles from –60 to 150 ºC, the sensors have proven stability and accuracy in responding to signals in a broad band from static to half a megahertz. Compared with conventional broadband sensors such as piezoelectric wafers, this genre of inkjet-printed nanocomposite sensors avoids the influence of increased dielectric permittivity during the measurement of high-frequency signals at elevated temperatures. Use of the sensors for characterizing undersized cracks in a typical aerospace structural component under acute temperature variation has spotlighted the alluring application potentials of the all-inkjet-printed nanocomposite sensors in implementing *in-situ* structural health monitoring for key aircraft and spacecraft components.

***Keywords*:** A. Nano composites; B. Thermal properties; D. Ultrasonic testing; E. Additive manufacturing; Structural health monitoring

1. Introduction

Structural health monitoring (SHM), a bionic paradigm inspired by the manner of signal perception and decision-making of human beings, has shown appealing promise in safeguarding engineering assets, and it has become a crucial building block in the holistic development of new generation of aircraft and spacecraft [1-4]. This sophisticated structural integrity-enhancement technique trans-disciplinarily embraces state-of-the-art scientific advances and technological breakthroughs in mechanics, material science, informatics, big data, sensing technology and additive manufacturing. Amidst diverse SHM approaches, acousto-ultrasonic wave-driven SHM, which leverages numerous merits of acousto-ultrasonic waves, has ushered in a new avenue to strike a balance among resolution, detectability, practicality and cost, corroborating the concept of *in-situ* SHM. By interpreting changes of subtle acousto-ultrasonic wave features, multiscale damage or fault in an inspected structure can be pinpointed and characterized, either qualitatively or quantitatively.

In an acousto-ultrasonic wave-driven SHM approach, the sensor network, either externally attached on a structural surface or internally embedded inside the structure, plays a rudimentary yet critical role in perceiving environmental variation and feature changes of waves guided by the inspected structure, in a "real-time" and *in-situ* manner [5-8], on which basis diagnosis and prognosis can be implemented [9-13]. However, irrespective of the intention of discovering damage and monitoring its progress, the deployment of such an approach and its supporting system on aircraft or spacecraft possibly introduce defect, stress concentration and incompatibility between sensors and the host structures, and in addition impose extra volume and weight penalty. This concern is particularly accentuated when stiff yet brittle sensors such as piezoceramic wafers are networked in a dense formality [14], and the inspected structure is manipulated in a cruel environment.

In recognition of these deficiencies and inspired by the booming nanotechnology, the authors have earlier developed a new breed of nanocomposite piezoresistive sensors for *in-situ*, acousto-ultrasonic wave-driven SHM [15, 16]. Under acousto-ultrasonic wave-induced strains, quantum tunneling effect generated in the formed nanofiller conductive network induces a dynamic alteration in the electrical conductivity and thus the piezoresistivity of the sensors, endowing the sensors with capacity in perceiving acousto-ultrasonic wave signals. This type of thin film-like sensors can be sprayable [5, 17] and printable [18, 19] to various structural surfaces, and tailor-made to resonate a specific frequency of the signal to be acquired by fine-tuning the degree of sensor conductivity [18]. The developed sensors feature values such as rapid prototyping, flexibility, lightweight and broadband response, blazing a new trail in developing *in-situ* SHM for aircraft and spacecraft.

On the other hand, aircraft and spacecraft are operated in extremely atrocious conditions with acute variation in ambient parameters including air pressure, humidity, and temperature, to name a few. Amongst various ambient parameters, temperature has been evidenced as one of the most influential factors to critically affect the performance of an SHM system and the sensors in particular [20]. The temperature of the operating environment for typical aircraft varies from –50 °C when they fly at a high altitude to 60 °C when park in a closed hangar. For spacecraft, tremendous heat flux induced during the re-entry to the Earth atmosphere elevates the temperature as high as ~1650 °C. Even with the thermal protection systems, the temperature of internal components in spacecraft soars to 150 °C. When orbiting, spacecraft undergo a drastic fluctuation in temperature (~70-100 °C) within a day when facing towards or away from the sun [21]. On top of that, the internal heat radiation from cabin electronics is another unneglectable hostile thermal factor which can negatively affect structural performance.

The aggressive environmental exposures not only degrade the performance of sensors *per se*, but also weaken the adhesion between sensors and the host structure. A thermal cycle as a result of acute change of ambient temperature progressively fatigues adhesive layers, potentially leading to exfoliation of sensors. In addition, thermal fluctuation alternately expands and contracts a structure, and changes material phase or chemical composition, jointly leading to deviation in material geometry and material properties including Young's modulus, Poisson's ratio and acoustic parameters (*e.g.*, transmitting velocity of the acousto-ultrasonic waves) [22]. Consequently, under the interference from temperature variation, the changes of signal features extracted by an SHM system, such as the arrival time of ultrasonic waves, may not faithfully reflect the health status of the inspected structure, leading to false alarm or ignorance of damage *de facto* [23, 24].

With the temperature effect in mind, the sensors used to implement *in-situ* SHM for aircraft or spacecraft must be rigorously selected, and sensor networks must be deliberately configured, so that a desired level of reliability and durability can be maintained within the entire range of temperature variation during operation. The rudimental requirements embrace: (i) the sensors to accommodate *in-situ* SHM of aircraft and spacecraft must be stable, durable and robust at severe operating temperature extremes, and able to withstand mechanical strain under severe operating conditions for a prolonged period; (ii) the sensitivity and accuracy of the sensors must not be compromised within the entire range of temperature fluctuation for a complete flight; (iii) compensation must be applied to correct contaminated signal features due to temperature variation; and (iv) sensors should maintain an adequate level of reliability after environmentally harsh storage, transit, and operation [25]. Driven by this, Blaise and Chang [26] investigated the performance of embedded piezoelectric transducers (PZT-5A, PZT denotes lead zirconate titanate) in capturing ultrasonic wave signals at low temperatures (–90 to 20 °C), and concluded that in this temperature variation range, ultrasonic wave signals can be reconstructed using an empirical linear model. Raghavan and Cesnik [21] examined the ultrasonic signal features captured by PZT-5A piezoelectric wafers from spacecraft structures subjected to a varying temperature from 20 to 150 °C, to reveal that under elevated temperature, time-of-flight (ToF) of the signal increases with temperature, and signal amplitude is affected by adhesion properties. Lanza di Scalea and Salamone [27] calibrated the responses of monolithic PZT patches and macrofibre composite (MFC) patches, when ambient temperature changed from –40 to 60 °C which corresponds to that change during a normal flight, and argued that for both PZT and MFC, the variations in ultrasonic wave signal amplitude follow two opposite trends below and above 20 °C, respectively. Several temperature compensation methods have also been proposed, to minimize the temperature effect, as typified by baseline signal stretch (BSS) [28], optimal baseline selection (OBS) [29], combination of BSS and OBS [30, 31], and combination of OBS and adaptive filter [32].

Nevertheless, prevailing studies on temperature effect on sensor performance are restricted to piezoceramics-type sensors, which have gain prominent popularity in developing SHM approaches for aircraft and spacecraft. The sensing performance of nanocomposite sensors under an extended range of temperature change has yet been attended hitherto. In this study, the temperature effect on nanocomposite piezoresistive sensors in acquiring broadband acousto-ultrasonic wave signals is investigated in an extensive temperature regime (–60 to 150 °C) that spans the thermal extremes undergone by typical aircraft and spacecraft. To this end, all-inkjet-printed (AIP) sensors, each featuring a thickness of only ∼1 μm, are fabricated using a drop-on-demand additive manufacturing approach. Making use of the quantum tunneling effect, the sensors are morphologically optimized at the nanoscale, to endow the sensors with adequate sensitivity to the ultrasonic waves with frequencies at half a megahertz – the frequencies predominantly adopted by acousto-ultrasonic wave-driven SHM. A theoretical model is developed to predict dispersive characteristics of acousto-ultrasonic waves at varying temperatures, against which the capability and accuracy of the sensors in perceiving broadband acousto-ultrasonic wave signals under harsh thermal cycles are examined experimentally. Results are also compared with commercial piezoelectric wafers. Taking a step further, a sensor network consisting of AIP sensors is configured to implement *in-situ* characterization of damage in a typical aerospace structural component under acutely varying temperatures.

2. Fabrication of AIP Sensors

2.1. Printing of Sensing Ink and Morphological Characterization

Central to the preparation of ink for developing nanocomposite piezoresistive sensors is the ink stability and printability, in addition to its functionality. Conductive carbon black (CB) powders (CABOT Black Pearl 2000, average particle diameter: 30 nm, as nanofiller) are mixed with polyvinylpyrrolidone (PVP, K-30, Sigma-Aldrich, as polymer matrix) at a weight ratio of 1:2 (0.28 g and 0.56 g, respectively) in 40 mL N-methyl-2-pyrrolidone (NMP, J&K Scientific). The dispersion of CB and PVP in NMP solvent is stabilized by adding 0.08 g sodium dodecylbenzenesulfonate (SDBS, Sigma-Aldrich, as surfactant). The mixture is mechanically stirred at 400 rpm for 2 hours at a room temperature (25 ºC), followed by a sonication for 1 hour in an ultrasonic bath. After sonication, the CB/PVP dispersion is filtered through a 0.45 μm-diameter polyvinylidene fluoride (PVDF) micropore sieve, to remove large CB/PVP agglomerates so that blockage and clogging of the inkjet printer nozzle can be avoided.

Such produced CB/PVP ink shows good stability, printability, and wettability. The ink is printed directly onto a substrate using a PiXDRO LP50 inkjet printer (OTB Solar-Roth & Rau) equipped with a DMC-11610 cartridge (Dimatix-Fujifilm Inc.). The printing process allows a sensor to be customizable in different patterns and printed passes, to accommodate various needs of sensing. Details of the sensing or printing process can be referred to the authors' early work [18]. In this study, each sensor, printed on the substrate with the sensing ink, measuring 10.0 mm in width and 20.0 mm in length, with 12 printed passes (leading to a total thickness of ~1.0 μm). The substrate is pre-treated with O_2 plasma prior to the printing process, endowing the substrate with high surface energy which is conducive to the improvement of wettability of the ink and good adhesion between sensors and the substrate. **Figure 1(a)** shows such produced sensors printed on a flexible heat-resistant polyimide (PI) film substrate, along with a typical SEM image of the printed sensor showing its morphology.

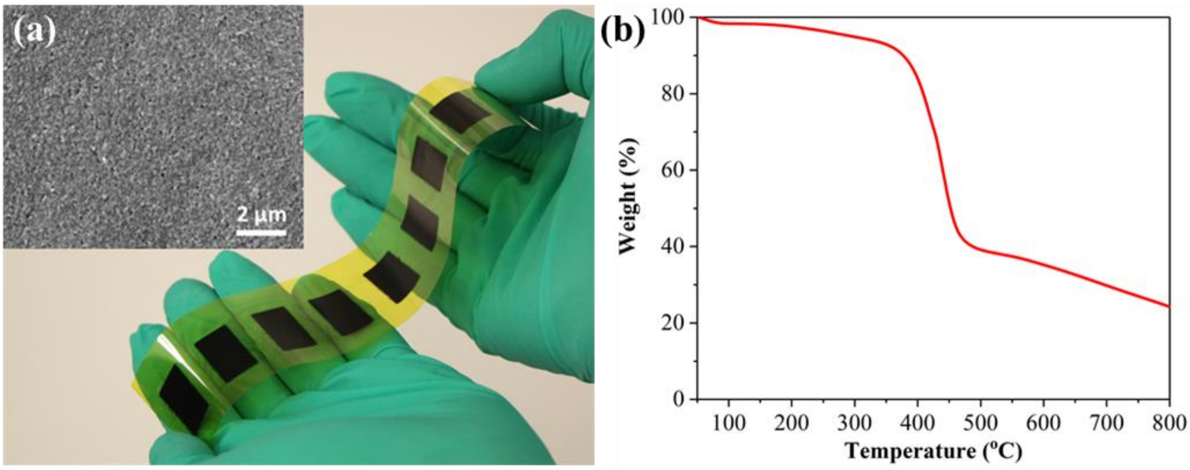

Fig. 1. (a) Inkjet-printed CB/PVP sensors on a PI film substrate (insert: SEM (20.00 k× magnification) image of the printed sensor); and (b) TGA curve of inkjet-printed CB/PVP sensors

Thermal stability of the printed nanocomposite sensors is calibrated through a thermalgravimetric analysis (TGA), using a TGA/DSC3+ (Mettler Toledo) system, to show the intrinsic thermal stability of the fabricated nanocomposites. In TGA, the proportion of remained mass/weight is measured over time as the temperature changes. The sensors are heated under an argon flow at 80 mL/min, from room temperature to 800 ^{o}C with a heating rate of 10 ^{o}C/min. As can be seen from **Fig. 1(b)**, the sensors remain their stability at a temperature as high as ~370 ^{o}C, since which the sensors tend towards initial decomposition, as ~370 ^{o}C is the decomposition temperature of PVP polymer.

2.2. Electrode and Insulating Layer Printing

Silver electrodes and insulating layers are installed onto the printed CB/PVP sensors via the same inkjet printing process, as illuminated by the flowchart shown in **Fig. 2(a)**. A pair of silver electrodes is inkjet-printed with commercial Metalon® JS-A211 silver ink (Novacentrix, 40.0 wt.% Ag, Average particle size: 36 nm) onto each sensor, with the gap of 2 mm between two electrodes. The printing resolution is set as 500 dpi in both cross-scan and in-scan directions (inkjet droplet spacing ~50 μm), which is the same as that of the sensor printing process, and the electrodes are fabricated with two printed passes. The AIP sensors with AIP electrodes are then heated on a hot plate at 140 ^{o}C for 10 mins, to accelerate the solvent evaporation and curing of the silver electrodes. Insulating layer is installed to prevent possible external interference or damage, such as short circuit and scratch. To fabricate the insulating layers, poly(pyromellitic dianhydride-*co*-4,4′-oxydianiline) amic acid (PAA) solution (12.8 wt.% (80% NMP/20% aromatic hydrocarbon), Sigma-Aldrich; 1g) is diluted in 19 mL NMP (J&K Scientific), followed with mechanical stirring at a room temperature for 15 mins at 800 rpm. The printing resolution is set as 600 dpi in both cross-scan and in-scan directions, higher than the sensor and electrode printing of 500 dpi, so that the inkjet droplet spacing is reduced to ~42 μm. The prepared PAA ink is then printed onto the surfaces of the sensors and electrodes using the same inkjet printing platform, after which the substrates are heated on a hot plate at 160 °C for 15 mins. Such a heating process is aimed at enabling the solvent evaporation and imidization of PAA [33] and consequently forming the insulating layer. The thermal imidization process of PAA is shown in **Fig. 2(b)**. With such a fabrication process, the nanocomposite-based AIP sensors are fabricated directly on either a flexible film or a structural surface. A multitude of such produced sensors can further be networked via inkjet-printed circuits developed with the same silver ink for electrodes, and **Fig. 2(c)** displays a paradigm of the sensor network configured by six AIP sensors deployed on a glass fibre reinforced plastic (GFRP) laminate.

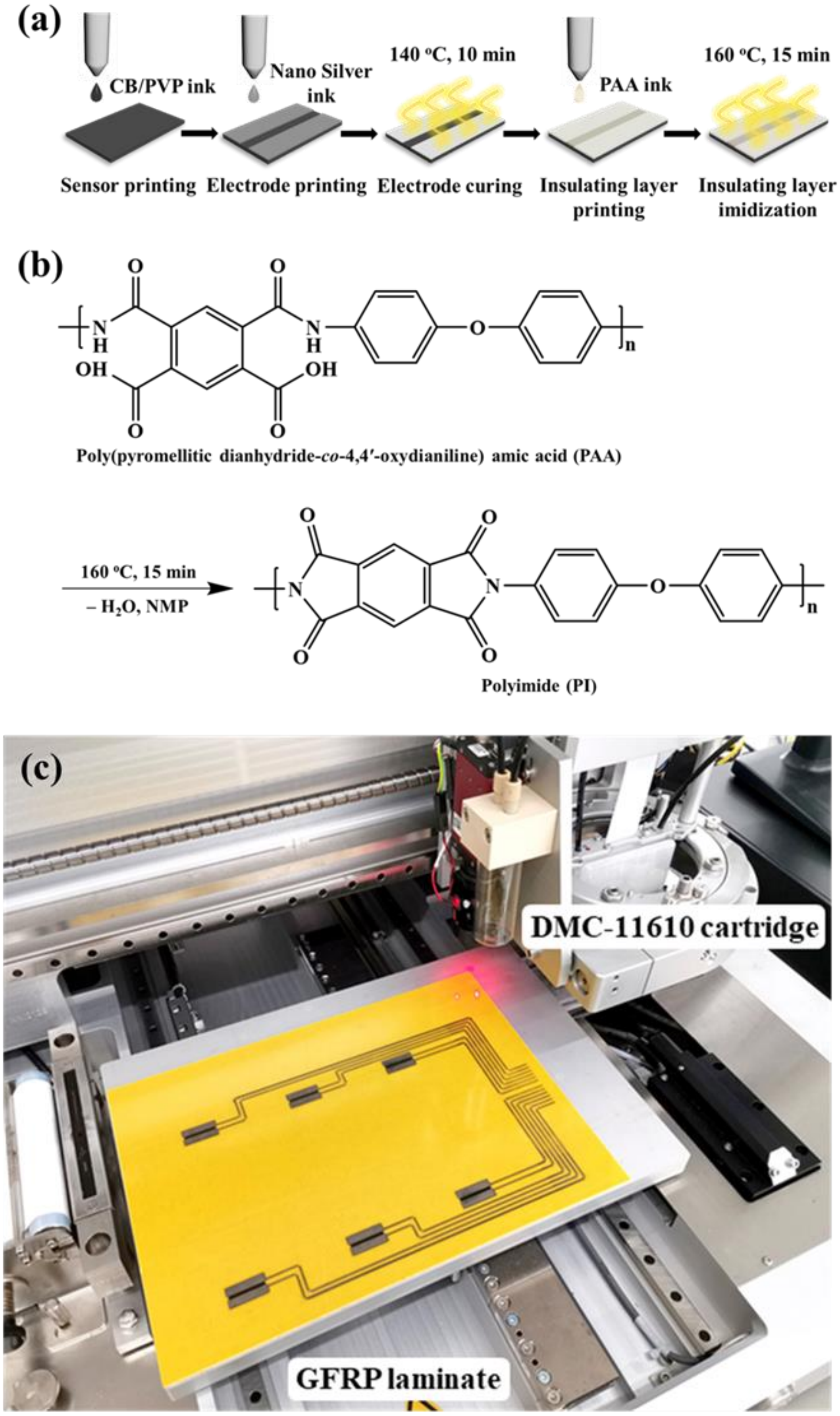

Fig. 2. (a) Process flow of electrode and insulating layer printing of AIP sensors; (b) thermal imidization process of PAA; and (c) AIP sensor network with printed circuits on a GFRP laminate.

3. Experiments, Results and Discussion

3.1. Sensing Capability at Varying Temperatures

The sensing capability of the developed AIP sensors in responding to broadband acousto-ultrasonic waves is examined in an extensive temperature regime (–60 to 150 ºC) that spans the thermal extremes undergone by typical aircraft and spacecraft. An aluminium alloy (6061-T6) plate (600 mm long and wide, 2 mm thick) is prepared, surface-bonded with a PZT wafer (PSN-33, Ø12 mm, 1 mm thick) that is used as an ultrasonic transmitter; an AIP sensor deposited on a PI film, produced as described in Section 2, is surface-glued on the plate, 210 mm apart from the PZT transmitter, for signal acquisition, as shown in **Fig. 3(a)**. Another surface-mounted PZT wafer is collocated alongside the AIP sensor, to capture counterpart signals for comparison. To securely bond the PZT wafers and the AIP sensor on the plate, the plate surface is roughened with light sanding and cleaned by acetone, and otherwise the weak bonding or bonding agent degradation under thermal cyclic loads can result in weak and inaccurate sensing or even exfoliation of sensors. The PZT wafers are adhered on the aluminium plate with a two-component epoxy (Epotek® 353ND, Epoxy Technology Inc.), while the AIP sensor is glued with single-component bonding agent (SELLEYS® Supa Glue Shock Proof) which is of a higher degree of operational simplicity. The use of different adhesives in this study is aimed at achieving the best bonding conditions for two different types of sensors. The adhesion and gluing are cured overnight at 20 ºC, and a light weight (500 g) is applied on each wafer and sensor to warrant adequate bonding.

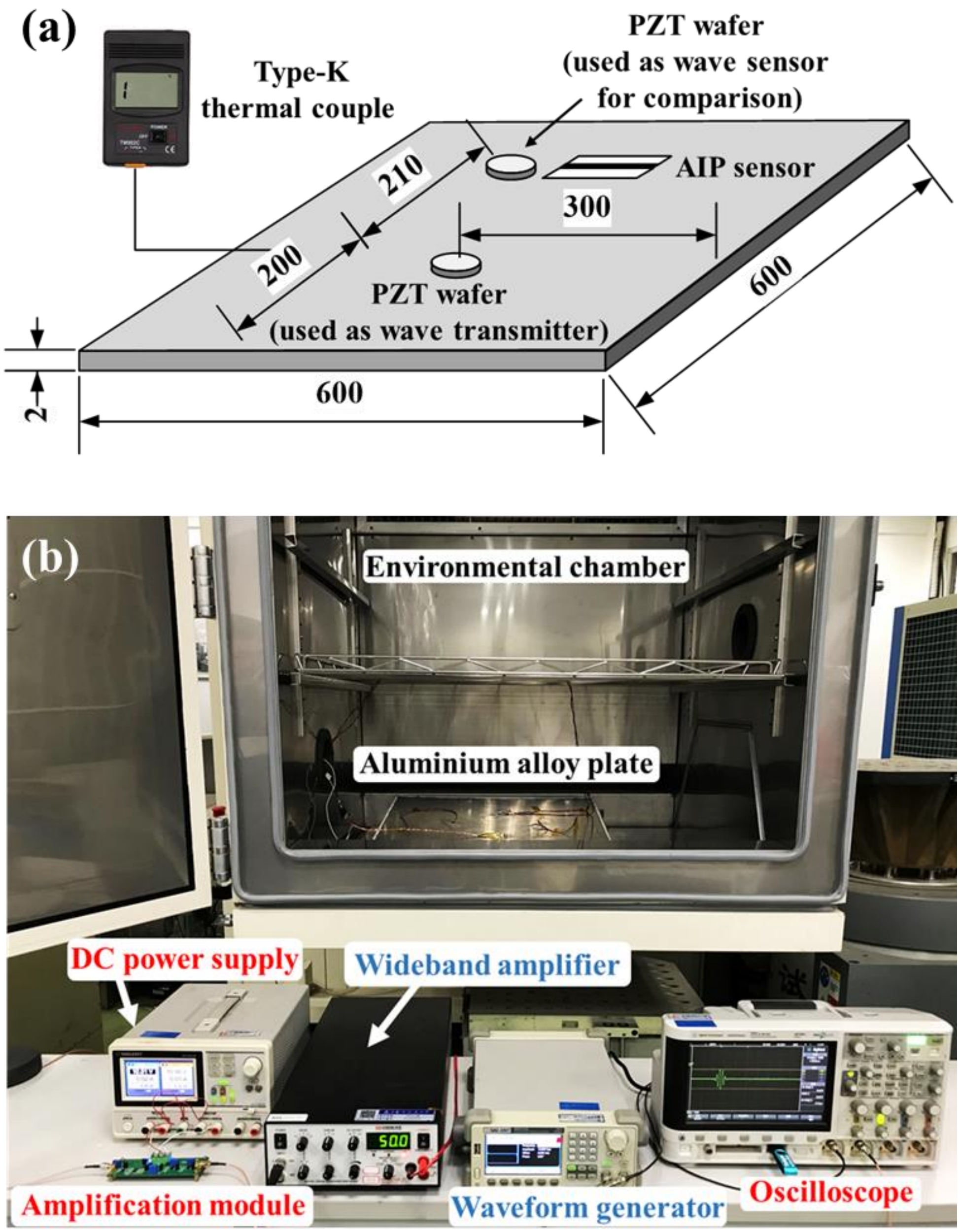

Fig. 3. (a) Schematic of experimental set-up for broadband acousto-ultrasonic wave acquisition (unit: mm); and (b) measurement system for ultrasonic wave acquisition under varying temperatures.

Acousto-ultrasonic wave signals are acquired at varying temperatures in a computer-controlled environmental chamber (THV1070W, Hongrui) which regulates the ambient temperature between –60 and 150 ºC precisely with a heating or cooling rate of 1 ºC/min.

The excitation signal is generated with an arbitrary waveform generator (SIGLENT SDG 5122) and amplified by a wideband amplifier (7602M, Krohn-Hite Corporation), taking a waveform of five-cycle Hanning-function-modulated sinusoidal tone-bursts with the central frequency ranging from 50 to 500 kHz (with an increment of 25 kHz). The excitation signal is applied on the PZT transmitter to emit acousto-ultrasonic waves into the aluminium plate. The signals are then captured by the AIP sensor. Temperature of the plate is measured with a type-K thermal couple (apuhua TM-902C), schematically illustrated in **Fig. 3(a)**. The sensor is connected to a self-developed amplification and signal conditioning module via shielded cables. In the module, a Wheatstone bridge converts piezoresistive variations to electrical signals. The converted signals and their counterpart signals captured by the PZT wafer are synchronously registered with a 4-channel digital oscilloscope (MSOX 3014A, Agilent Technologies). The electrical resistances of electrical cables and connections in the measurement system are negligible, as copper electrical cables, not affecting the sensing performance of the fabricated sensors.

To facilitate evaluation of the sensor stability under different temperatures and also the comparison against PZT wafer, key signal features, embracing ToF, signal phase and amplitude, are extracted from acquired signals. Here, ToF is defined as the time difference between (i) the peak of the first wave component (the zeroth-order symmetric Lamb wave mode guided by the aluminium plate, denoted by S_0 hereinafter) in a signal and (ii) the peak of the excitation, either in the time domain or in the spectrogram obtained with the short-time Fourier transform, with an example, when the ambient temperature is 20 ^{o}C, shown in **Fig. 4**.

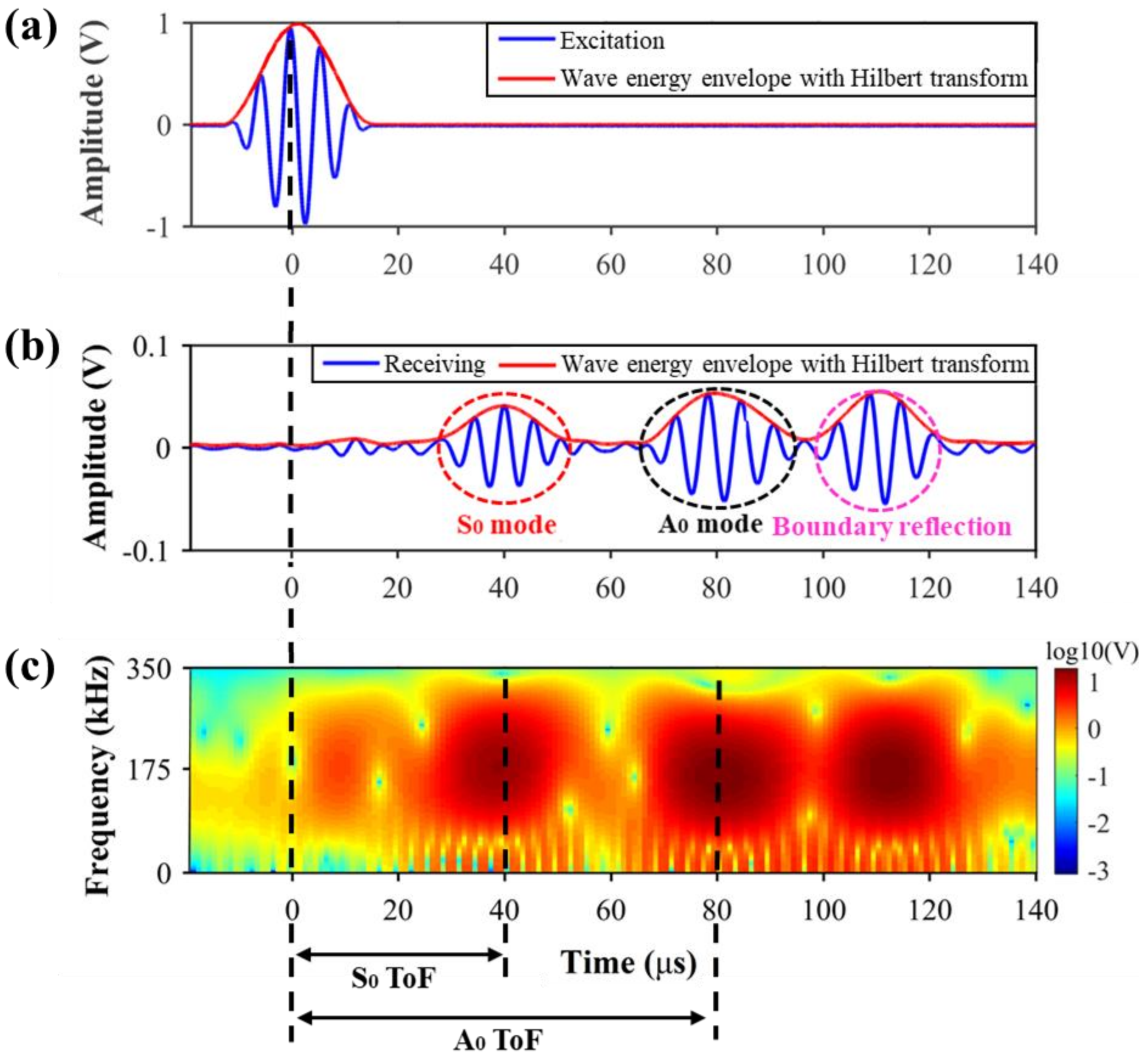

Fig. 4. Measurement of ToF of acousto-ultrasonic wave signal captured by the AIP sensor at 20 ºC: (a) excitation signal with central frequency of 175 kHz; (b) signal captured by the AIP sensor; and (c) spectrogram of signal in (b) shown in a logarithmic scale.

Figure 5 compares signals, when the wave is excited at 175 and 500 kHz (heating or cooling), respectively – as two representative cases, and perceived by the AIP sensor in a thermal cycle. For each signal depicted in **Fig. 5**, the signal amplitude is normalized to the peak value of the S_0 mode. The AIP sensor is observed to maintain its high sensitivity to acousto-ultrasonic wave-induced strains in an extensive temperature regime from –60 to 150 ºC, and also in a broad frequency band from static to half a megahertz (viz., the frequency that is predominantly adopted by acousto-ultrasonic wave-driven SHM). During the thermal cycle, both the S_0 mode and the other wave modes (*e.g.*, the zeroth-order anti-symmetric Lamb wave mode guided by the aluminium plate, denoted by A_0 hereinafter), as well as reflected signals from the plate boundary, are faithfully perceived by the AIP sensor, with clear waveforms and high signal-to-noise ratio (SNR).

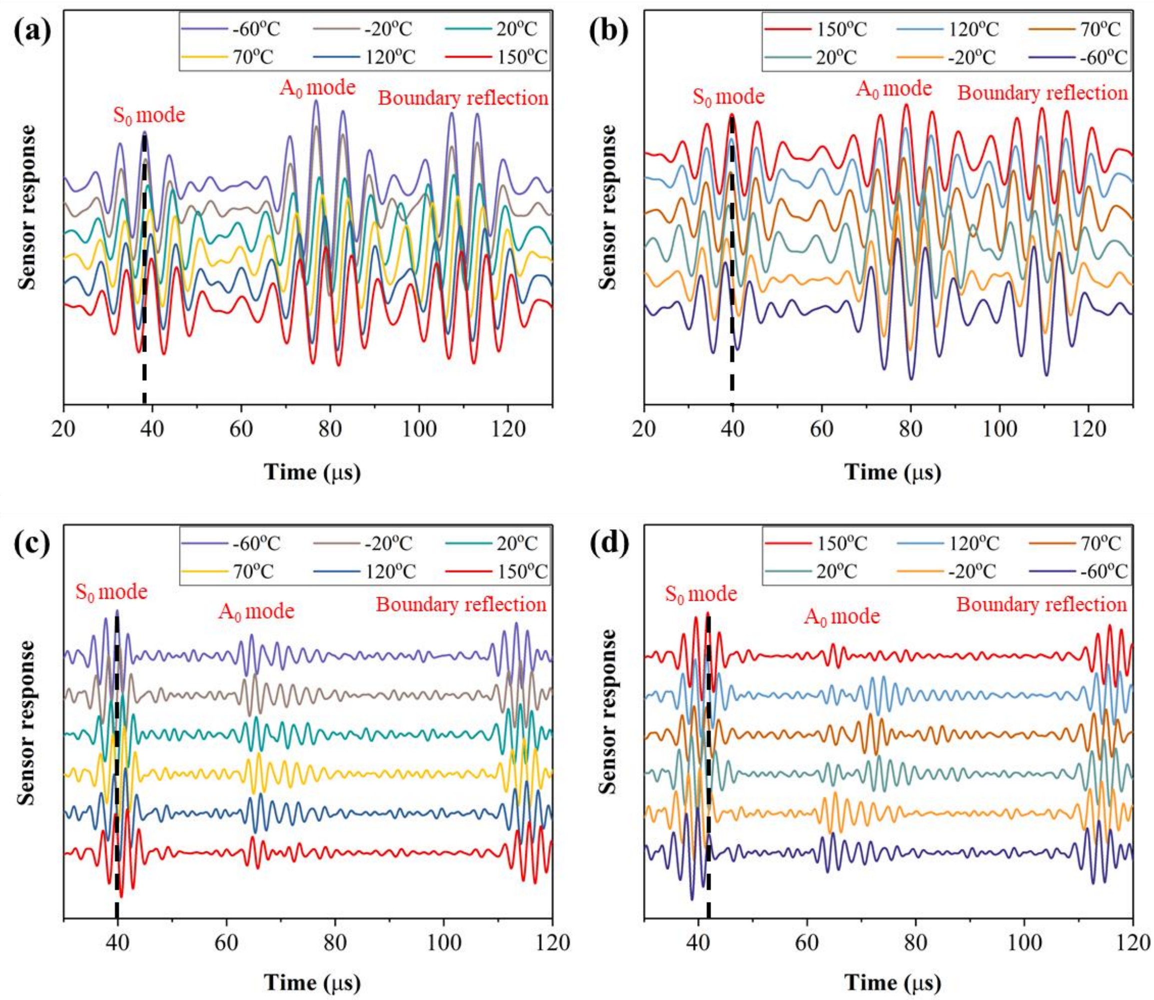

Fig. 5. Acousto-ultrasonic wave signals captured by the AIP sensor under varying temperatures in a thermal cycle at an excitation frequency of: (a) 175 kHz (heating); (b) 175 kHz (cooling); (c) 500 kHz (heating) and (d) 500 kHz (cooling).

It is interesting to note in **Fig. 5** that in a thermal cycle, either at its heating or cooling semi-period, a higher temperature results in a greater ToF, and *vice versa*. To examine such a phenomenon in an extended range, **Fig. 6(a)** compares the extracted ToFs of signals captured in three thermal cycles, when the wave is excited at 175 kHz as a typical case. The error bars in the figure illustrate the variation in ToF at a certain temperature in different thermal cycles. ToFs in **Fig. 6(a)** show the same tendency as that when piezoelectric sensors are used for acousto-ultrasonic wave acquisition, as reported elsewhere [21, 27, 34].

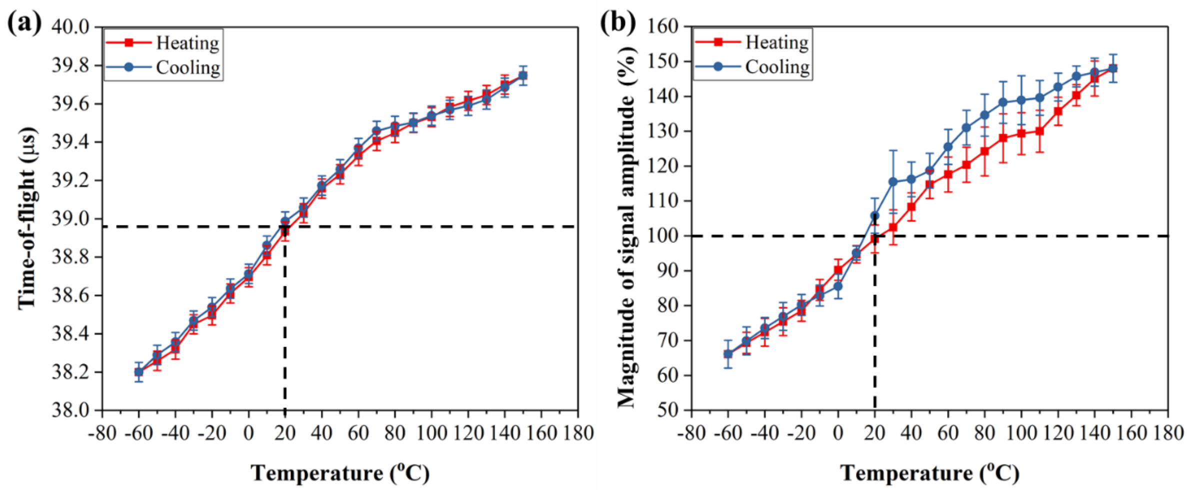

Fig. 6. (a) ToF and (b) amplitude of the AIP sensor-captured acousto-ultrasonic wave signals under varying temperatures (excitation frequency: 175 kHz).

As far as the signal amplitude concerned, **Fig. 6(b)** depicts the change of signal amplitude in three thermal cycles, and the plot is normalized to the signal amplitude measured at 20 °C before the thermal cycles for comparison. As can be seen from **Fig. 6(b)**, in both heating and cooling stages, a higher temperature leads to a larger signal amplitude, and *vice versa*. From the results shown in **Fig. 6**, the ToF and amplitude of the signal perceived by the AIP sensor are observed highly consistent throughout the entire range of interested temperatures, indicating that not only the bonding is suitable and robust, but the fabricated sensors are stable and functional under an extreme thermal variation from –60 to 150 °C, with comparable performance as commercial piezoelectric sensors.

The variation in signal amplitude at different temperatures, **Fig. 6(b)**, is attributed to the variation of piezoelectric coefficient of PZT wafer with temperature. For the PZT wafer used as wave transmitter in this study, the acousto-ultrasonic wave-induced dynamic strain ε generated by the converse piezoelectric effect of the wafer can be estimated via [35]

$$\varepsilon = d_{31}K_3 = -d_{31}\frac{V}{h_{\mathrm{PZT}}}, \tag{1}$$

where d_{31} denotes the in-plane piezoelectric coefficient of the PZT wafer, K_3 the applied out-of-plane electric field, V the applied external voltage, and h_{PZT} the thickness of the wafer. When the operation temperature is no more than half of the Curie temperature (half the Curie temperature for PSN-33 wafers is 167.5 °C), the wafer remains functional and the absolute value of d_{31} increases with temperature [36]. As can be seen from Eq. (1), the acousto-ultrasonic wave-induced strain increases with larger d_{31}, and the consequence is that within the temperature range from –60 to 150 °C, the higher the temperature in the aluminium plate, the larger the strain will be generated. For the AIP sensor – a type of piezoresistive sensor, at a higher temperature, although the tunneling gap is narrowed [37], a larger strain induced by the wave causes more conductive network destruction within the CB-formed conductive network in PVP. A higher degree of tunnel-conductive path destruction in the sensor leads to higher sensitivity to external strains, and as a result, stronger signal amplitude is perceived at higher temperature.

It is noteworthy that in previous studies [27, 34] where piezoelectric sensors are used for acousto-ultrasonic wave acquisition, at higher temperatures above 20 °C, the captured signal amplitude becomes weaker as temperature increases, and this phenomenon is also observed in the present study: the amplitude of signal perceived by the PZT sensor at 175 kHz dropped by ~60% at 150 ^{o}C, when compared to that measured at 20 ^{o}C before the thermal cycles. This can be attributable to the competing interaction between the increasing absolute value of the piezoelectric coefficient and the dielectric permittivity in the PZT wafer [38, 39]. These findings argue that the AIP sensor can avoid the negative influence of increased dielectric permittivity in conventional piezoelectrical measurement at a high temperature – an advantage of the AIP sensor over those conventional piezoelectric sensors (such as PZT wafers) in acquisition of broadband acousto-ultrasonic waves at extensive thermal conditions.

3.2. Sensing Precision at Varying Temperatures

Sensing precision of the developed AIP sensors in responding to broadband acousto-ultrasonic waves, subjected to varying temperatures, is scrutinized. First, it is of relevance and necessity to advance the understanding of temperature effect of the measurement system. As discussed in Section 3.1, the bonding layer is proven stable and robust within the discussed temperature variation range (–60 to 150 ^{o}C). Therefore, the properties of the bonding layer can be considered to be constant, and the change of bonding layer thickness (less than 0.01 mm) by thermal expansion is negligible [34]. For the configured experiment in which the PZT wafer is used as a wave transmitter, the change of ambient temperature, according to Eq. (1), only alters the strain magnitude of an excited wave. Altogether, the variation in transmitting velocity of the wave guided by the aluminium plate and then in the ToF of the wave propagation can be solely attributable to the changes in plate properties and geometry under varying temperatures. To put such changes into perspective, consider an infinite isotropic plate, in which the temperature-dependent acousto-ultrasonic wave motion is governed by [40]

$$(\lambda(T)+\mu(T))\nabla(\nabla\vec{u})+\mu(T)\nabla^2\vec{u}+\rho(T)\vec{f}=\rho(T)\ddot{\vec{u}}, \tag{2}$$

where

$$\lambda(T)=\frac{E(T)\nu(T)}{\big(1+\nu(T)\big)\big(1-2\nu(T)\big)}, \tag{3}$$

$$\mu(T)=\frac{E(T)}{2\big(1+\nu(T)\big)}. \tag{4}$$

In the above, $\vec{u}$ denotes the displacement vector, $\vec{f}$ the body force, and T the temperature. λ and μ signify the two Lame's elastic moduli that are related to the Young's modulus E and Poisson's ratio ν. ρ is the mass density, which is also temperature-dependent and can be ascertained by solving the differential equation that is defined as (valid at constant pressure P) [34]

$$\left(\frac{\partial\rho(T)}{\partial T}\right)_P+\rho(T)\alpha_V=0, \tag{5}$$

where α_V is the volumetric thermal expansion coefficient of the plate.

Guided to propagate in the plate, the propagating velocity of acousto-ultrasonic waves of various modes, including the above-mentioned S_0 and A_0 modes, are of a dispersive nature, showing strong dependence on wave excitation frequency, which can be depicted as [41]

$$\frac{\tanh(qh)}{\tanh(ph)}=-\left[\frac{4k^2pq}{(q^2-k^2)^2}\right]^{\pm1}, \tag{6}$$

where

$$p=\sqrt{(\omega/c_L)^2-k^2}, \tag{7}$$

$$q=\sqrt{(\omega/c_T)^2-k^2}. \tag{8}$$

In Eq. (6), +1 in the exponent is for the symmetric modes, and -1 for the antisymmetric modes. In Eqs. (6)-(8), ω is the angular frequency of the acousto-ultrasonic waves. k denotes the wavenumber, and h half-thickness of the plate and which are related to bulk transverse propagating velocity c_T and longitudinal velocity c_L of the acousto-ultrasonic waves. c_T and c_L are defined as

$$c_T = \sqrt{\frac{E}{2\rho(1+\nu)}}, \tag{9}$$

$$c_L = \sqrt{\frac{E(1-\nu)}{\rho(1+\nu)(1-2\nu)}}. \tag{10}$$

According to Eqs. (9) and (10), it is noteworthy that the wave dispersion lies jointly upon the Young's modulus, Poisson's ratio and density of the plate. All these properties vary with temperature in a linear manner as [27]

$$R(T) = R(T_0) + \frac{\partial R(T)}{\partial T}\Delta T, \tag{11}$$

where R signifies one of the three properties (*i.e.*, Young's modulus, Poisson's ratio or density of the plate), T_0 the original ambient temperature (20 ºC in this study), and $\partial R(T)/\partial T$ the sensitivity of the property with regard to the change of ambient temperature.

3.2.1. Theoretical Prediction of Dispersive Characteristics of Waves at Varying Temperatures

Without loss of generality, 6061-T6 aluminium plates discussed in Section 3.1 are considered. Key material properties of the plates at 20 ºC as well as their sensitivities to the change of ambient temperature (i.e., $\partial R(T)/\partial T$) [34, 42] are listed in **Table 1**, and these parameters are recalled to analytically estimate the dispersive characteristics of waves via Eqs. (6) and (11).

Table 1 Key material properties of 6061-T6 aluminium plate at 20 °C and their sensitivity to change of ambient temperature

Material properties	Values at 20 °C	Sensitivities to temperature
Young's modulus (E)	$E(T_0) = 71.16$ GPa	$\partial E(T)/\partial T = -27.00 \times 10^{-3}$ GPa/°C
Poisson's ratio (ν)	$\nu(T_0) = 0.33$	$\partial \nu(T)/\partial T = 54.79 \times 10^{-6}$/°C
Density (ρ)	$\rho(T_0) = 2700$ kg/m^3	$\partial \rho(T)/\partial T = -1.87 \times 10^{-1}$ kg/m^3/°C

The dispersion natures, reflected in terms of the phase and group velocities of the acousto-ultrasonic waves versus temperature variation, obtained using Eqs. (6) and (11), are shown in **Fig. 7**, in the regime from –60 to 150 °C. The phase velocity is referred to as the propagation speed of the phase of a particular frequency contained in the wave, while the group velocity is the velocity with which the overall shape of the wave amplitude, which is the actual velocity captured in experiment. Phase and group velocities of both the fundamental S_0 and A_0 modes show a downward trend with higher temperatures. It is noteworthy that within the temperature range of interest, the changes in wave dispersion are remarkable – a phenomenon that is attributed to change of mechanical properties of the plate under temperature effect. A higher temperature leads to an increase of material compliance with a subsequent reduction of the acousto-ultrasonic wave propagating speeds, which in turn reduces the phase and group velocities of wave modes. The trend of the ToF variation shown in **Fig. 6(a)** – a higher temperature leading to a greater change of ToF, can thus be explained by the velocity change of the dispersive waves.

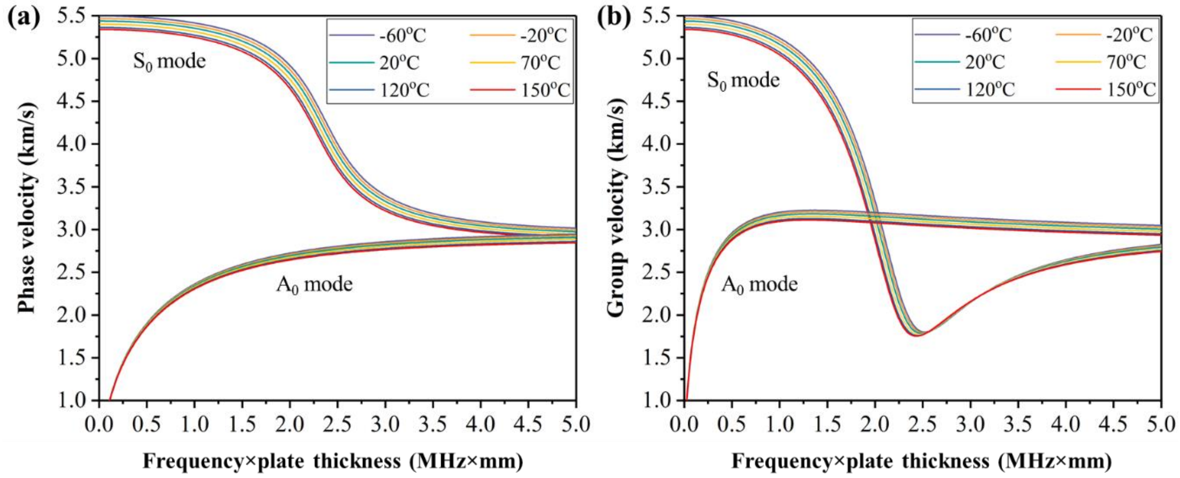

Fig. 7. Dispersion curves of waves in an isotropic 6061-T6 aluminium plate at different temperatures: (a) phase velocity and (b) group velocity.

3.2.2. Experimental Validation

The above theoretical estimate of the propagation characteristics of acousto-ultrasonic waves subjected to temperature change (from –60 to 150 ºC) is further experimentally validated. With all parameters remained identical to those in the above theoretical prediction, the ToFs of S_0 and A_0 wave modes are measured using the experimental set-up shown in **Fig. 3(b)**, and the group velocities are calculated. Compared with experimental measurement using the collocated PZT sensor (for the purpose of comparison) and results from previous studies [21, 34, 42] where piezoelectric wafers are used as wave sensors, the analytical prediction is proven accurate in estimating the dispersive characteristics of acousto-ultrasonic waves at varying temperatures. As shown in **Fig. 8,** the experimentally obtained group velocities of both the S_0 and A_0 modes by the AIP sensor decrease as the temperature increases, showing good consistency with the trend of dispersion nature calculated theoretically in the preceding section. These findings have confirmed that the nanocomposite-based AIP sensors are able of acquiring broadband acousto-ultrasonic wave signals in an extensive temperature regime responsively, precisely and stably, with comparable performance as commercial piezoelectric sensors.

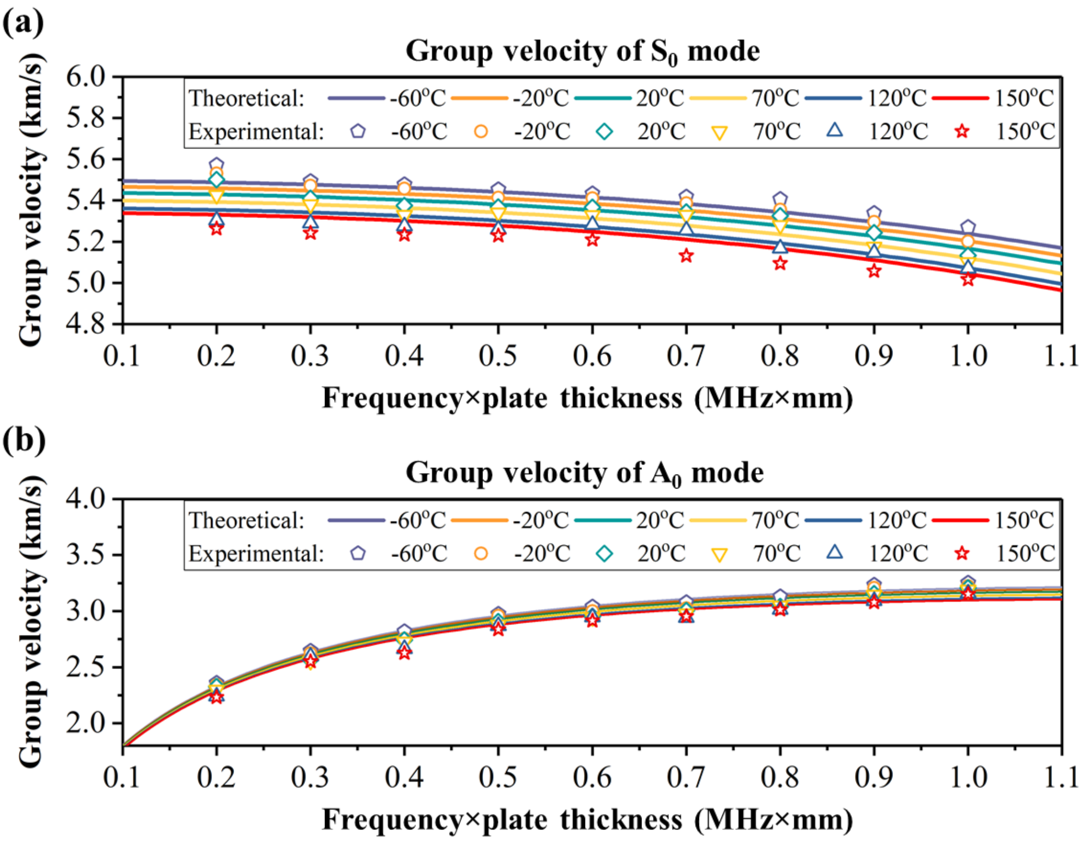

Fig. 8. Comparison of theoretically obtained dispersion curves and experimentally obtained dispersion curves with the AIP sensor: (a) S_0 and (b) A_0 modes.

4. An Application Paradigm: Damage Characterization Using Acousto-ultrasonic Waves at Varying Temperatures

Upon material morphological investigation, nano-structural optimization and sensing performance validation, the developed nanocomposite-based AIP sensors are extended to damage characterization using high-frequency elastic waves at varying temperatures. As shown in **Fig. 9**, eight thus-produced AIP sensors (serving as broadband acousto-ultrasonic wave sensors) and two PZT wafer (used as wave actuators) are surface-mounted on an isotropic 6061-T6 aluminium plate, to configure a circular sensing network which renders in total 16 actuator-sensor paths. A through-thickness crack of 20 mm in length and 2 mm in width is pre-introduced to the plate using a fine blade, at the location of (-22.5 mm, 22.5 mm). A seven-cycle Hanning-windowed sinusoidal tone-burst at a central frequency of 175 kHz is applied to drive each PZT actuator in turn to generate probing acousto-ultrasonic waves via an arbitrary waveform generator and wideband amplifier. Measurement procedures remain the same as those described in Section 3.1.

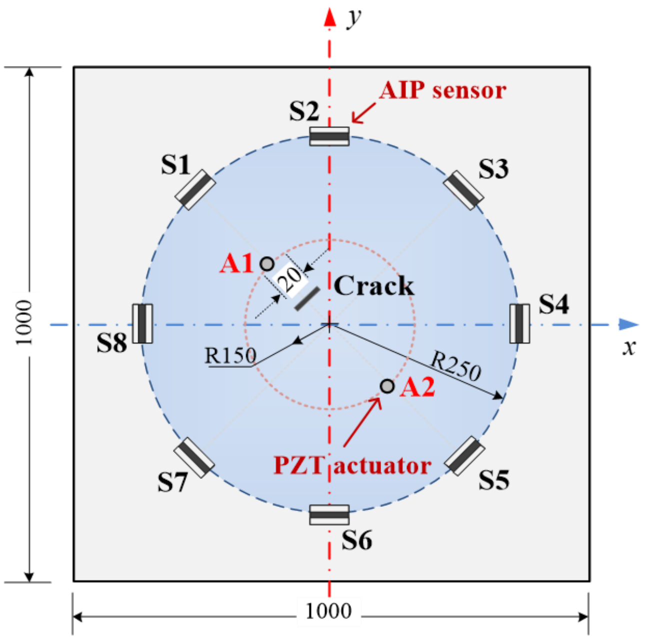

Fig. 9. Schematic of the 6061-T1 aluminium plate with a fine crack, on which a sensing network is configured with eight AIP sensors and two PZT wafers (A*i* and S*i* denote PZT actuator and AIP sensor, respectively; unit: mm).

Two representative sets of signals acquired via the actuator-sensor path A2-S5, at 20 and 60 °C, before and after introducing the crack to the plate, are presented in **Fig. 10**. In these signals, the first and second wave packets are the incipient acousto-ultrasonic wave modes (*i.e.*, S_0 and A_0 modes). The third wave packet in the signals obtained in the damaged plate, but not observed in the baseline signals from the pristine plate, is the wave component converted from the incipient S_0 mode when it is scattered by the damage, and this wave packet is named as damage-scattered S_0 mode.

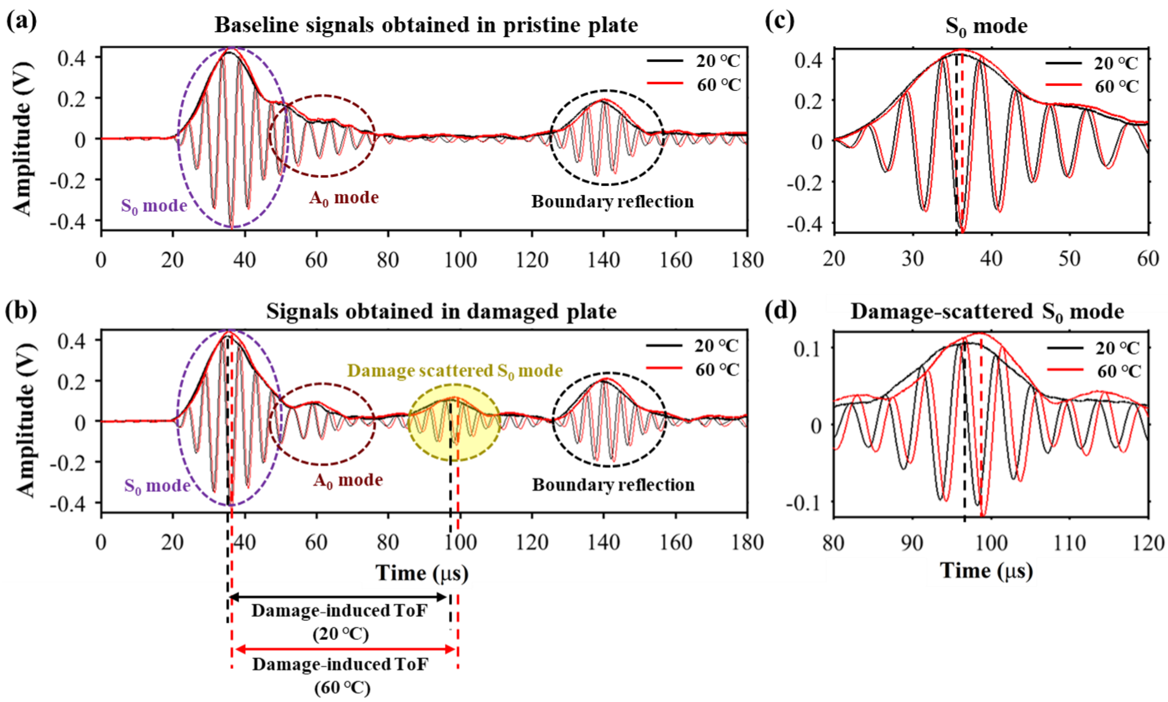

Fig. 10. Signals captured via actuator-sensor path A2-S5: (a) before (baseline signals obtained in pristine plate) and (b) after a fine crack is introduced; and comparison of wave packets in signals captured at 20 and 60 °C: (c) S_0 mode and (d) damage-scattered S_0 mode.

Damage-induced ToF, as indicated in **Fig. 10(b)**, is extracted from the signals for damage localization via a triangulation algorithm [43], in terms of the relative position of the actuator Ai (x_{A_i}, y_{A_i}), AIP sensor Si (x_{S_i}, y_{S_i}) and damage D (x_D, y_D), as

$$\left(\frac{L_{A_i-D}+L_{D-S_i}}{v_0}\right)-\frac{L_{A_i-S_i}}{v_0}=\Delta t_i, (i=1,2,\ldots N), \quad (12)$$

where

$$L_{\mathrm{A}_i-\mathrm{D}} = \sqrt{(x_{\mathrm{A}_i} - x_{\mathrm{D}})^2 + (y_{\mathrm{A}_i} - y_{\mathrm{D}})^2}, \quad (13)$$

$$L_{\mathrm{D}-\mathrm{S}_i} = \sqrt{(x_{\mathrm{D}} - x_{\mathrm{S}_i})^2 + (y_{\mathrm{D}} - y_{\mathrm{S}_i})^2}, \quad (14)$$

$$L_{\mathrm{A}_i-\mathrm{S}_i} = \sqrt{(x_{\mathrm{A}_i} - x_{\mathrm{S}_i})^2 + (y_{\mathrm{A}_i} - y_{\mathrm{S}_i})^2}. \quad (15)$$

In Eqs. (12)-(15), $L_{\mathrm{A}_i-\mathrm{D}}$, $L_{\mathrm{D}-\mathrm{S}_i}$ and $L_{\mathrm{A}_i-\mathrm{S}_i}$ denote the distances from the actuator Ai $(x_{\mathrm{A}_i}, y_{\mathrm{A}_i})$ to the damage centre D $(x_{\mathrm{D}}, y_{\mathrm{D}})$, from the damage centre to the sensor Si $(x_{\mathrm{S}_i}, y_{\mathrm{S}_i})$, and from the actuator to the sensor, respectively. v_0 is the group velocity of the incipient S_0 mode. Δt_i (*i.e.*, damage-induced ToF) is to be determined from the signal captured by the actuator-sensor path Ai-Si. By solving Eq. (12) with the knowledge of v_0, $(x_{\mathrm{A}_i}, y_{\mathrm{A}_i})$ and $(x_{\mathrm{S}_i}, y_{\mathrm{S}_i})$, an elliptical locus with two foci at the actuator Ai and sensor Si can be ascertained (see **Fig. 11**), implying all the possible locations of damage in this actuator-sensor path. With more elliptical loci from all the available 16 actuator-sensor paths, the damage location $(x_{\mathrm{D}}, y_{\mathrm{D}})$ can be determined by mathematically seeking the intersection of these ellipses.

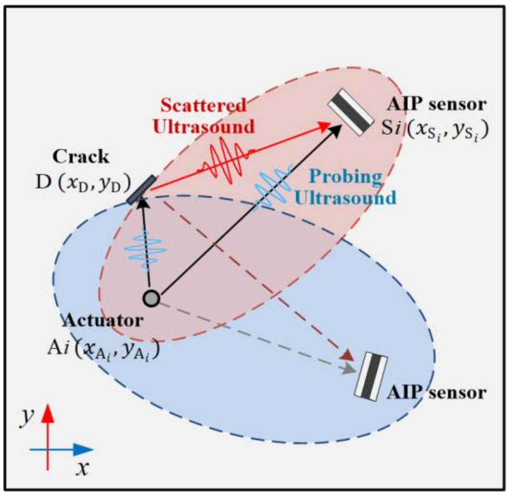

Fig. 11. Relative positions of the actuator Ai, AIP sensor Si, and damage D in an actuator-sensor path.

A probability-based diagnostic imaging (PDI) algorithm [44, 45] is recalled, using all data from the two actuators for data fusion to visualize the identified damage in a two-dimensional greyscale image, with results shown in **Fig. 12** for two scenarios when the experiments are performed at 20 and 60 °C. PDI presents the diagnostic results in terms of the probability of presence of damage in the inspected structure, with detailed description in the authors' previous work [46]. Points on a particular locus that produced by an actuator-sensor path are of the highest degree of probability (100%) of damage presence, while for other points the probability of damage presence decreases with the distance to the locus. For a specific point in the diagnostic image, a higher field value with outstanding pixel suggests a higher probability of damage presence, which gives users an intuitive and precise perception of the damage location.

In **Fig. 12(a)**, the diagnostic image constructed with the ToF-based PDI, when the group velocity of the waves obtained at 20 °C is used, quantitatively tallies with the reality. However, as discussed in Section 3.2, the group velocity of waves varies as temperature changes, which may lead to pseudo or erroneous diagnostic results if the temperature effect is not taken into account and compensated. At 60 °C, compensation for temperature-dependent wave group velocity is applied, based on the dispersion curves obtained at 60 °C in Section 3.2. Only with such compensation can precise identification of the damage be achieved, with results shown in **Figs. 12(b) and (c)**. The imaging result in **Fig. 12(c)** shows high coincidence with the true location and the crack orientation, affirming the performance of the developed AIP sensor in *in-situ* SHM applications at varying temperature conditions.

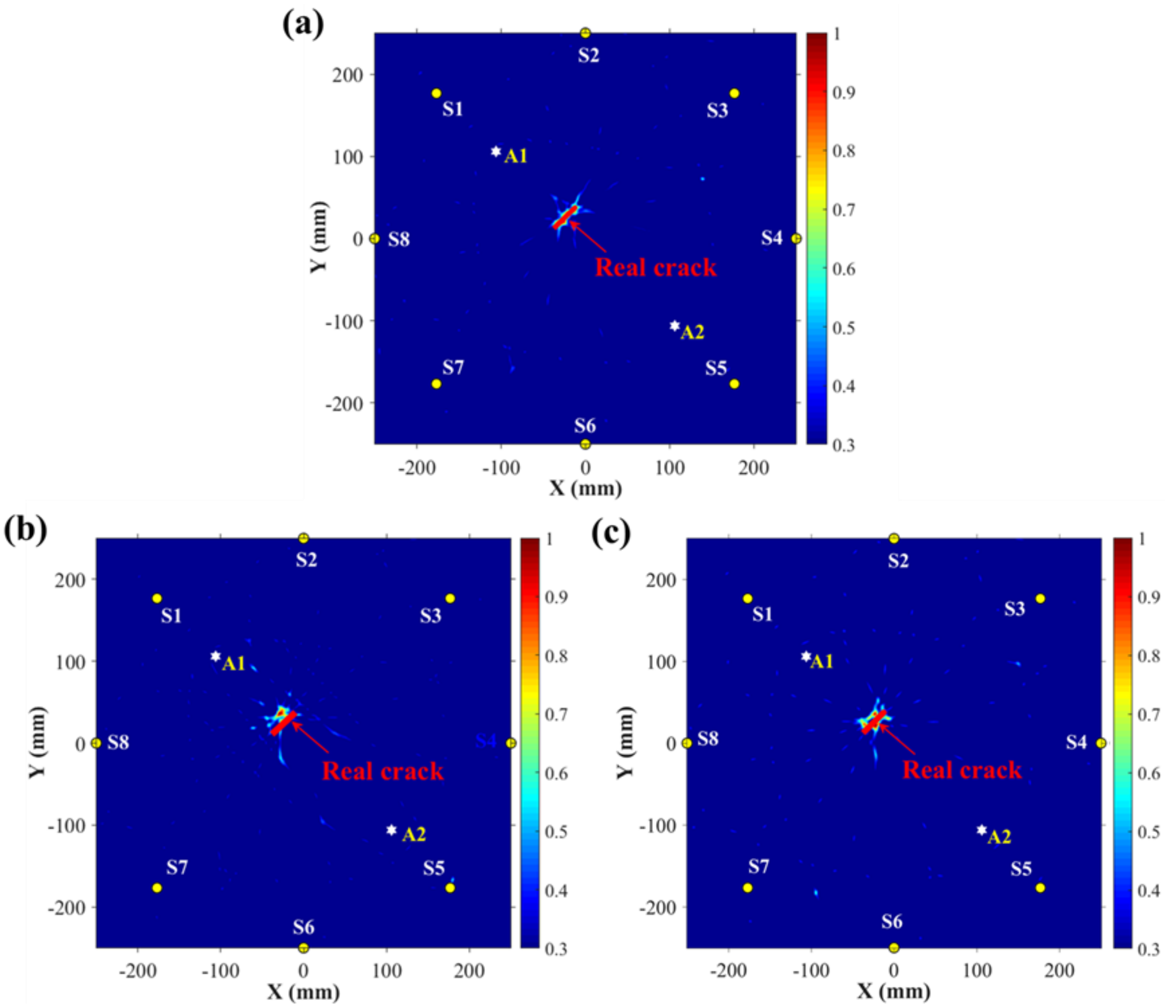

Fig. 12. Diagnostic images obtained with ToF-based PDI algorithm at: (a) 20 °C; (b) 60 °C (without temperature compensation) and (c) 60 °C (with temperature compensation).

5. Concluding Remarks

The temperature effect on the nanocomposite-based AIP sensors in acquiring broadband acousto-ultrasonic wave signals is examined in an extensive temperature regime (–60 to 150 °C) that spans the thermal extremes undergone by typical aircraft and spacecraft. A new genre of nanocomposite-based piezoresistive sensors is developed in virtue of quantum tunneling effect, using a drop-on-demand additive manufacturing approach – inkjet printing, and optimized to precisely respond to ultraweak disturbance induced by acousto-ultrasonic waves at half a megahertz – the frequencies predominantly adopted by acousto-ultrasonic wave-driven SHM. The AIP sensors have been demonstrated capable in perceiving acousto-ultrasonic wave signals under harsh thermal cycles. The dispersive characteristics of waves acquired by the sensors at varying temperatures exhibit good consistency with the theoretical model. With proven sensing accuracy and sensitivity comparable to commercial piezoelectric sensors, the AIP sensors outperform piezoelectric sensors with an additional merit that the negative influence of increased dielectric permittivity during measurement of high-frequency signals at elevated temperatures can be prevented. These findings have confirmed that the AIP sensors are of good stability and high degree of sensing precision within a wide range of temperature variation. AIP sensor network configured with a multitude of AIP sensors is deployed to perform *in-situ* characterization of damage in a typical aerospace structural component under acutely varying temperatures, highlighting the alluring application potentials of the developed AIP nanocomposite sensors in fulfilling *in-situ* structural health monitoring for key aircraft and spacecraft components at harsh thermal conditions. The influence of variations in other ambient parameters will be explored in subsequent studies.

Acknowledgments

The work was supported by a General Project (No. 51875492) and a Key Project (No. 51635008) received from the National Natural Science Foundation of China. The authors acknowledge the support from the Hong Kong Research Grants Council via General Research Funds (Nos. 15204419 and 15212417). The authors thank the State Key Laboratory of Mechanics and Control of Mechanical Structures, Nanjing University of Aeronautics and Astronautics for supporting the environmental chamber in this research.

References

[1] S. Yuan, Y. Ren, L. Qiu, H. Mei, A Multi-Response-Based Wireless Impact Monitoring Network for Aircraft Composite Structures, IEEE Transactions on Industrial Electronics 63(12) (2016) 7712-7722.

[2] N.D. Alexopoulos, C. Bartholome, P. Poulin, Z. Marioli-Riga, Structural Health Monitoring of Glass Fiber Reinforced Composites Using Embedded Carbon Nanotube (CNT) Fibers, Composites Science and Technology 70(2) (2010) 260-271.

[3] S. Salamone, I. Bartoli, F. Lanza Di Scalea, S. Coccia, Guided-wave Health Monitoring of Aircraft Composite Panels under Changing Temperature, Journal of Intelligent Material Systems and Structures 20(9) (2009) 1079-1090.

[4] S. Makireddi, S. S, G. Kosuri, F.V. Varghese, K. Balasubramaniam, Electro-elastic and Piezoresistive Behavior of Flexible MWCNT/PMMA Nanocomposite Films Prepared by Solvent Casting Method for Structural Health Monitoring Applications, Composites Science and Technology 118 (2015) 101-107.

[5] W. Cao, P. Zhou, Y. Liao, X. Yang, D. Pan, Y. Li, B. Pang, L.-m. Zhou, Z. Su, A Spray-on, Nanocomposite-Based Sensor Network for in-situ Active Structural Health Monitoring, Sensors 19(9) (2019).

[6] L. Qiu, S. Yuan, X. Zhang, Y. Wang, A Time Reversal Focusing Based Impact Imaging Method and Its Evaluation on Complex Composite Structures, Smart Materials and Structures 20(10) (2011) 105014.

[7] D.G. Aggelis, N.M. Barkoula, T.E. Matikas, A.S. Paipetis, Acoustic Structural Health Monitoring of Composite Materials : Damage Identification and Evaluation in Cross Ply Laminates Using Acoustic Emission and Ultrasonics, Composites Science and Technology 72(10) (2012) 1127-1133.

[8] K. Xu, D. Ta, Z. Su, W. Wang, Transmission Analysis of Ultrasonic Lamb Mode

Conversion in a Plate with Partial-thickness Notch, Ultrasonics 54(1) (2014) 395-401.

[9] S. Yuan, X. Lai, X. Zhao, X. Xu, L. Zhang, Distributed Structural Health Monitoring System Based on Smart Wireless Sensor and Multi-agent Technology, Smart Materials and Structures 15(1) (2005) 1-8.

[10] W. Qiang, Y. Shenfang, Baseline-free Imaging Method Based on New PZT Sensor Arrangements, Journal of Intelligent Material Systems and Structures 20(14) (2009) 1663-1673.

[11] M. Liu, Z. Zeng, H. Xu, Y. Liao, L. Zhou, Z. Zhang, Z. Su, Applications of a Nanocomposite-inspired in-situ Broadband Ultrasonic Sensor to Acousto-ultrasonics-based Passive and Active Structural Health Monitoring, Ultrasonics 78 (2017) 166-174.

[12] Y. Wang, L. Qiu, Y. Luo, R. Ding, A Stretchable and Large-scale Guided Wave Sensor Network for Aircraft Smart Skin of Structural Health Monitoring, Structural Health Monitoring (2019) 1475921719850641.

[13] J.-X. Shi, T. Natsuki, X.-W. Lei, Q.-Q. Ni, Wave Propagation in the Filament-wound Composite Pipes Conveying Fluid: Theoretical Analysis for Structural Health Monitoring Applications, Composites Science and Technology 98 (2014) 9-14.

[14] Y. Wang, Y. Luo, L. Qiu, Simulation Method of an Expandable Lamb Wave Sensor Network for Aircraft Smart Skin, IEEE Sensors Journal 20(1) (2020) 102-112.

[15] Z. Zeng, M. Liu, H. Xu, W. Liu, Y. Liao, H. Jin, L. Zhou, Z. Zhang, Z. Su, A Coatable, Light-weight, Fast-response Nanocomposite Sensor for the in situ Acquisition of Dynamic Elastic Disturbance: from Structural Vibration to Ultrasonic Waves, Smart Materials and Structures 25(6) (2016) 065005.

[16] Z. Zeng, M. Liu, H. Xu, Y. Liao, F. Duan, L.-m. Zhou, H. Jin, Z. Zhang, Z. Su, Ultra-broadband Frequency Responsive Sensor Based on Lightweight and Flexible Carbon

Nanostructured Polymeric Nanocomposites, Carbon 121 (2017) 490-501.

[17] Y. Liao, F. Duan, H. Zhang, Y. Lu, Z. Zeng, M. Liu, H. Xu, C. Gao, L.-m. Zhou, H. Jin, Z. Zhang, Z. Su, Ultrafast Response of Spray-on Nanocomposite Piezoresistive Sensors to Broadband Ultrasound, Carbon 143 (2019) 743-751.

[18] P. Zhou, Y. Liao, Y. Li, D. Pan, W. Cao, X. Yang, F. Zou, L.-m. Zhou, Z. Zhang, Z. Su, An Inkjet-printed, Flexible, Ultra-broadband Nanocomposite Film Sensor for in-situ Acquisition of High-frequency Dynamic Strains, Composites Part A: Applied Science and Manufacturing 125 (2019) 105554.

[19] Y. Liao, P. Zhou, D. Pan, L.-m. Zhou, Z. Su, An Ultra-thin Printable Nanocomposite Sensor Network for Structural Health Monitoring, Structural Health Monitoring (2019) 1475921719859338.

[20] H. Sohn, Effects of Environmental and Operational Variability on Structural Health Monitoring, Philosophical Transactions of the Royal Society A: Mathematical, Physical and Engineering Sciences 365(1851) (2007) 539-560.

[21] A. Raghavan, C.E.S. Cesnik, Effects of Elevated Temperature on Guided-wave Structural Health Monitoring, Journal of Intelligent Material Systems and Structures 19(12) (2008) 1383-1398.

[22] W. Li, A. Dichiara, J. Zha, Z. Su, J. Bai, On Improvement of Mechanical and Thermo-mechanical Properties of Glass Fabric/epoxy Composites by Incorporating CNT–Al_2O_3 Hybrids, Composites Science and Technology 103 (2014) 36-43.

[23] X. Qing, W. Li, Y. Wang, H. Sun, Piezoelectric Transducer-Based Structural Health Monitoring for Aircraft Applications, Sensors 19(3) (2019).

[24] A. Mohimi, T.-H. Gan, W. Balachandran, Development of High Temperature Ultrasonic Guided Wave Transducer for Continuous in Service Monitoring of Steam Lines Using Non-stoichiometric Lithium Niobate Piezoelectric Ceramic, Sensors and

Actuators A: Physical 216 (2014) 432-442.

[25] A. Baker, N. Rajic, C. Davis, Towards a Practical Structural Health Monitoring Technology for Patched Cracks in Aircraft Structure, Composites Part A: Applied Science and Manufacturing 40(9) (2009) 1340-1352.

[26] E. Blaise, F. Chang, Built-in Diagnostics for Debonding in Sandwich Structures under Extreme Temperatures, Proceedings of the 3rd international workshop on structural health monitoring, Stanford, California, USA, 2001, pp. 154-163.

[27] F. Lanza di Scalea, S. Salamone, Temperature Effects in Ultrasonic Lamb Wave Structural Health Monitoring Systems, The Journal of the Acoustical Society of America 124(1) (2008) 161-174.

[28] Y. Lu, J.E. Michaels, A Methodology for Structural Health Monitoring with Diffuse Ultrasonic Waves in the Presence of Temperature Variations, Ultrasonics 43(9) (2005) 717-731.

[29] G. Konstantinidis, B.W. Drinkwater, P.D. Wilcox, The Temperature Stability of Guided Wave Structural Health Monitoring Systems, Smart Materials and Structures 15(4) (2006) 967-976.

[30] T. Clarke, P. Cawley, P.D. Wilcox, A.J. Croxford, Evaluation of the Damage Detection Capability of a Sparse-array Guided-wave SHM System Applied to a Complex Structure under Varying Thermal Conditions, IEEE Transactions on Ultrasonics, Ferroelectrics, and Frequency Control 56(12) (2009) 2666-2678.

[31] T. Clarke, F. Simonetti, P. Cawley, Guided Wave Health Monitoring of Complex Structures by Sparse Array Systems: Influence of Temperature Changes on Performance, Journal of Sound and Vibration 329(12) (2010) 2306-2322.

[32] Y. Wang, L. Gao, S. Yuan, L. Qiu, X. Qing, An Adaptive Filter–based Temperature Compensation Technique for Structural Health Monitoring, Journal of Intelligent

Material Systems and Structures 25(17) (2014) 2187-2198.

[33] K.-i. Fukukawa, M. Ueda, Recent Progress of Photosensitive Polyimides, Polymer Journal 40(4) (2008) 281-296.

[34] A. Marzani, S. Salamone, Numerical Prediction and Experimental Verification of Temperature Effect on Plate Waves Generated and Received by Piezoceramic Sensors, Mechanical Systems and Signal Processing 30 (2012) 204-217.

[35] Z. Su, L. Ye, Activating and Receiving Lamb Waves, in: Z. Su, L. Ye (Eds.), Identification of Damage Using Lamb Waves: From Fundamentals to Applications, Springer London, London, 2009, pp. 59-98.

[36] H.-J. Lee, D.A. Saravanos, The Effect of Temperature Dependent Material Properties on the Response of Piezoelectric Composite Materials, Journal of Intelligent Material Systems and Structures 9(7) (1998) 503-508.

[37] R. Zhang, Y. Bin, R. Chen, M. Matsuo, Evaluation by Tunneling Effect for the Temperature-dependent Electric Conductivity of Polymer-carbon Fiber Composites with Visco-elastic Properties, Polymer Journal 45(11) (2013) 1120-1134.

[38] F. Lanza di Scalea, H. Matt, I. Bartoli, The Response of Rectangular Piezoelectric Sensors to Rayleigh and Lamb Ultrasonic Waves, The Journal of the Acoustical Society of America 121(1) (2007) 175-187.

[39] Sukesha, R. Vig, N. Kumar, Effect of Electric Field and Temperature on Dielectric Constant and Piezoelectric Coefficient of Piezoelectric Materials: A Review, Integrated Ferroelectrics 167(1) (2015) 154-175.

[40] Waves in Plates, in: J.L. Rose (Ed.), Ultrasonic Guided Waves in Solid Media, Cambridge University Press, Cambridge, 2014, pp. 76-106.

[41] Z. Shen, S. Chen, L. Zhang, K. Yao, C.Y. Tan, Direct-Write Piezoelectric Ultrasonic Transducers for Non-Destructive Testing of Metal Plates, IEEE Sensors Journal

17(11) (2017) 3354-3361.

[42] J.C. Dodson, D.J. Inman, Thermal Sensitivity of Lamb Waves for Structural Health Monitoring Applications, Ultrasonics 53(3) (2013) 677-685.

[43] Z. Su, L. Ye, Lamb Wave Propagation-based Damage Identification for Quasi-isotropic CF/EP Composite Laminates Using Artificial Neural Algorithm: Part II - Implementation and Validation, Journal of Intelligent Material Systems and Structures 16(2) (2005) 113-125.

[44] H. Sohn, H.J. Lim, M.P. DeSimio, K. Brown, M. Derriso, Nonlinear Ultrasonic Wave Modulation for Online Fatigue Crack Detection, Journal of Sound and Vibration 333(5) (2014) 1473-1484.

[45] Q. Wang, M. Hong, Z. Su, An In-Situ Structural Health Diagnosis Technique and Its Realization via a Modularized System, IEEE Transactions on Instrumentation and Measurement 64(4) (2015) 873-887.

[46] Y. Li, Y. Liao, Z. Su, Graphene-functionalized Polymer Composites for Self-sensing of Ultrasonic Waves: an Initiative towards “Sensor-free” Structural Health Monitoring, Composites Science and Technology 168 (2018) 203-213.